Ultrasound in Med. & Biol., Vol. 43, No. 3, pp. 648–661, 2017

0301-5629/$ - see front matter

http://dx.doi.org/10.1016/j.ultrasmedbio.2016.11.003

● *Original Contribution*

STRAIN-INITIALIZED ROBUST BONE SURFACE DETECTION IN 3-D ULTRASOUND

Mohammad Arafat Hussain,* Antony J. Hodgson,† and Rafeef Abugharbieh*

*Department of Electrical and Computer Engineering, University of British Columbia, Vancouver, British Columbia, Canada; and †Department of Mechanical Engineering, University of British Columbia, Vancouver, British Columbia, Canada

(*Received* 13 *July* 2016; *revised* 21 *October* 2016; *in final form* 2 *November* 2016)

Abstract—Three-dimensional ultrasound has been increasingly considered as a safe radiation-free alternative to radiation-based fluoroscopic imaging for surgical guidance during computer-assisted orthopedic interventions, but because ultrasound images contain significant artifacts, it is challenging to automatically extract bone surfaces from these images. We propose an effective way to extract 3-D bone surfaces using a surface growing approach that is seeded from 2-D bone contours. The initial 2-D bone contours are estimated from a combination of ultrasound strain images and envelope power images. Novel features of the proposed method include: (i) improvement of a previously reported 2-D strain imaging-based bone segmentation method by incorporation of a depth-dependent cumulative power of the envelope into the elastographic data; (ii) incorporation of an echo decorrelation measure-based weight to fuse the strain and envelope maps; (iii) use of local statistics of the bone surface candidate points to detect the presence of any bone discontinuity; and (iv) an extension of our 2-D bone contour into a 3-D bone surface by use of an effective surface growing approach. Our new method produced average improvements in the mean absolute error of 18% and 23%, respectively, on 2-D and 3-D experimental phantom data, compared with those of two state-of-the-art bone segmentation methods. Validation on 2-D and 3-D clinical *in vivo* data also reveals, respectively, an average improvement in the mean absolute fitting error of 55% and an 18-fold improvement in the computation time. (E-mail: arafat@ece.ubc.ca) **© 2016 World Federation for Ultrasound in Medicine & Biology.**

Key Words: **Ultrasound, Bone, Strain imaging, Segmentation, Gaussian mixture Regression, Surface growing.**

INTRODUCTION

Navigation systems in orthopedic surgery procedures often rely on intra-operative fluoroscopy for registering pre-operatively acquired models (*e.g.,* from computed tomography [CT] imaging) with the intra-operative anatomy. However, the associated radiation poses potential hazards to both the surgical staff and patients (Park et al. 2012). Over the past decade or so, intra-operative ultrasound (US) has been proposed as a safer alternative (Amin et al. 2003; Brendel et al. 2002; Brounstein et al. 2011; Chen et al. 2005; Foroughi et al. 2007; Hacihaliloglu et al. 2008, 2011). However, because of the very low signal-to-noise ratio (SNR), US images are comparatively difficult to interpret (Krissian et al. 2007). Typically, US beams strongly reflect from stiffer tissue surfaces such as bones, so these surfaces appear as bright ridge-like shapes in US images. However, other tissue layers can also produce similar intensity profiles, so it can be difficult to automatically distinguish between bone and soft tissue boundaries (Hussain et al. 2014), which would be necessary if US-based bone surface localization is to be used in practical intra-operative applications.

Over the last two decades, a number of semi-automatic and automatic methods for bone segmentation in US were developed based on morphologic features (Stindel et al. 2002; Tonetti et al. 2001), image gradients (Barratt et al. 2006; Daanen et al. 2004; Kowal et al. 2007), and active shape models (Alfiansyah et al. 2006; Jain and Taylor 2004). However, results were strongly affected by the high levels of speckle noise, reverberation, anisotropy, and signal dropout that occur in US images (Hacihaliloglu et al. 2012a, 2014). Dynamic programming-based methods (Foroughi et al. 2007; Patwardhan et al. 2012) also appear promising, but were reported to be time inefficient; for example, the method of Patwardhan et al. (2012), which was

Address correspondence to: Mohammad Arafat Hussain, 2329 West Mall, Vancouver, BC V6T 1Z4, Canada. E-mail: arafat@ece.ubc.ca

implemented in C++, took ~5 min to extract 3-D bone surfaces in an US volume of 200 × 100 × 100 voxels. More recently, work on using phase-based features for US bone segmentation by Hacihaliloglu et al. (2008, 2011, 2012a, 2012b) has successfully addressed some of the major limitations of the previously reported methods.

Hacihaliloglu et al. used a log Gabor filtering-based ridge detection approach to delineate bone in US images. This method used filters responsive to the angular orientations of bone found in the US images. Because soft tissue interfaces near the transducer face often exhibit intensity profiles similar to those of bone and frequently have similar angular orientations, this approach can occasionally produce false-positive responses (Hussain et al. 2014). The authors attempted to address this issue by adopting bottom-up ray casting (based on the assumption that the bone interface would be the deepest strong interface in the volume set), along with manual image cropping, but this approach may not be reliable or practical in a surgical environment. In addition, phase-based methods may also fail to extract bone boundaries in places where B-mode intensities are not sufficiently strong (*e.g.,* in places where the bone surface is not perpendicular to the US beam direction).

An alternative approach would be to exploit detection of the high mechanical stiffness of bone using US elastography (Hussain et al. 2014; Xu and Salcudean 2007). Xu and Salcudean (2007) were the first group to use US elastography to delineate bone surfaces in US images. However, their strain imaging-based method produced low contrast in the bone surface region, so the bone surface could not be accurately located. More recently, we proposed an improved method (Hussain et al. 2014) that employs real-time strain imaging to estimate the bone boundary using a tissue stiffness map. This approach enabled us to accurately estimate the location of the bone surface (within 0.75 mm on a phantom specimen). In short, the steps of our previous work were: (i) producing strain and envelope power maps using the raw radiofrequency (RF) data, (ii) fusing the strain and envelope power maps using an empirically chosen weight and (iii) producing final bone contours by linear regression over the maximum intensity points along each scan line in the fused map. However, this method is highly sensitive to the quality of the strain image, and relies on a manually defined weight that controls the relative contribution of the strain image in the bone boundary detection procedure. It also lacks the ability to detect bone discontinuities, and accurate delineation of the final bone surface is sensitive to the proper choice of the window length for local linear regression. In addition, this method was only able to detect the bone surfaces in 2-D US images.

In the study described here, we significantly enhanced our previous work by (i) incorporating a depth-dependent cumulative power of the envelope metric into both pre- and post-compression raw RF data before estimating the strain map, (ii) incorporating an echo decorrelation metric to choose a weight automatically that fuses the strain and envelope power maps and (iii) using a local statistics-based bone discontinuity detection scheme. In addition, we propose a 3-D bone segmentation approach for US that uses the estimated 2-D strain to identify a seed bone contour that is then grown in the elevation direction by minimizing a combined intensity similarity and a voxel proximity-based cost function. The performance of this algorithm is evaluated using a finite-element model (FEM) phantom, an experimental phantom and *in vivo* data, and is compared with the performance of two recent image phase feature-based bone boundary estimation algorithms.

METHOD

Our proposed strain enhancement method has three major components, as illustrated in Figure 1: (i) a customized scanning procedure, (ii) 2-D bone contour estimation procedure and (iii) 3-D bone surface extraction procedure using the surface growing approach.

Scanning procedure

Our algorithm combines a 2-D elastographic image with a standard 3-D B-mode volumetric scan. These images are acquired in two steps: (i) acquisition of 2-D pre- and post-compression RF frames, I_1 and I_2, respectively, (of size $m \times n$), where the US beam direction is nominally perpendicular to the bone surface, and (2) acquisition of 3-D US RF data (consisting of z frames) as the transducer sweeps over the target. To implement this approach, we use a 4-D linear array transducer that initially collects a number of 2-D US RF frames (axial × lateral) with freehand compression while the transducer array is positioned in the middle of its sweep (*i.e.,* in the probe's central plane). Once we are satisfied with the quality of the elastography data, we begin acquiring the 3-D US data by switching the transducer to the sweeping mode without removing it from the skin surface. The transducer sweeps in the elevation direction and acquires a volume. Note that we presume that the person performing the scan has sufficient experience to decide if the acquired images are of sufficient quality to produce an acceptable strain image.

2-D bone contour estimation

Background. To estimate the bone surface location in the pair of 2-D images, we used a real-time strain imaging technique developed by Rivaz et al. (2011), which is based on an analytic minimization of a regularized cost function defined as (pseudo-equation)

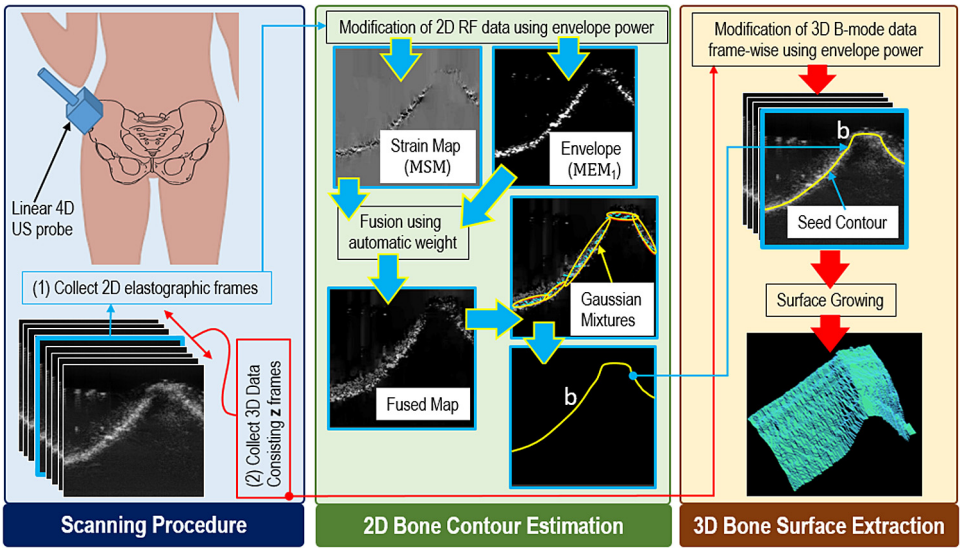

Fig. 1. Schematic indicating different components of our proposed method.

$$\text{cost} = \text{intensity similarity} + \text{displacement regularization} \tag{1}$$

The resulting strain image was fused with the envelope power map using a weight. The weight was selected based on an empirical analysis of the mean absolute error (MAE) between the actual and estimated bone surfaces for different weight values. The weight for which the MAE was lowest in this pilot data set was used throughout our experiments. Then we used local linear fits over the maximum intensity point along each scan line of the fused map to produce the final bone boundary. However, Rivaz et al. also mentioned an inherent limitation of their method: Weaker RF echoes cause a significant increase in the share of the regularization term in eqn (1), which results in oversmoothing of the strain image. In our work, we exploited this phenomenon to improve the bone delineation accuracy, as discussed in the next section.

2-D strain and envelope power map estimation. The work described here was focused on improving bone detection accuracy by improving the performance of strain and envelope power estimates. We devised a modification process for the raw RF data, which is used before estimating the strain map (see Fig. 1). Because the RF echoes and their envelopes are already weaker beneath the bone surface because of the very high US beam reflection at the bone–soft tissue interface (a simulated example is provided in Fig. 2a), we further modified the envelope map by reducing the intensity associated with the soft tissue region (area between the bone and the transducer face) using the axially cumulative power (see Fig. 2b) and produced modified envelope maps (see Fig. 2c), MEM_1 and MEM_2 from I_1 and I_2, respectively, as

$$\text{MEM}_r(i,j) = \frac{E_r(i,j)^{P_r(i,j)}}{\max\left[E_r(i,j)^{P_r(i,j)}\right]} \tag{2}$$

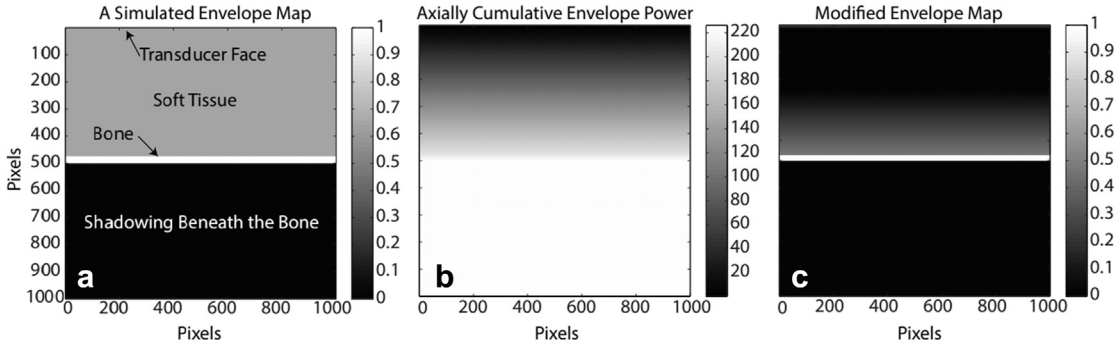

Fig. 2. (a) Simulated envelope map. (b) Axially cumulative envelope power of the map in (a). (c) Modification of the envelope map in (a) by the power map in (b) using eqn (2).

where r corresponds to 1 and 2, denoting the pre- and post-compression images, respectively; i and j denote the axial and lateral sample numbers, respectively; E_r is the envelope of I_r estimated using the Hilbert transform (Hussain et al. 2012b); and $P_r(i,j) = \sum_{p_o=1}^{i} E_r^2(p_o,j)$. Finally, we estimate strain (**S**) from the pre- and post-compression data pair MEM_1 and MEM_2 using the method developed by Rivaz et al. (2011). Consequently, an oversmoothing of both the top and bottom regions of the bone boundary in the resulting strain image occurs for the same reason discussed in the previous section (see the modified strain map in the midblock of Fig. 1). For robust bone boundary estimation, we further combine **S** with MEM_1. Because of the echo de-correlation in the freehand elastography, strain images often become very noisy. On the other hand, the envelope magnitude of the RF data is generally expected to be higher over the bone surfaces, but this is often not the case where the bone surface is not perpendicular to the US beam direction. Therefore, we combine information from both the strain and envelope power maps to complement one another. To ensure that the dynamic range of **S** is comparable to that of MEM_1, we define a modified strain map by normalizing **S**: $MSM = |\mathbf{S}|/\max[|\mathbf{S}|]$.

Fused map estimation. Next we fuse the MSM and MEM_1 as

$$FM = \lambda \times MSM + (1-\lambda) \times MEM_1 \tag{3}$$

where λ controls the contribution of MSM to the fused map. In our previous work (Hussain et al. 2014), the value of λ was chosen empirically. In this work, we incorporate the echo decorrelation measure between the pre- and post-compression RF frames to automatically choose a suitable value for λ. To do this, we first estimate the normalized cross-correlation ρ_{avg} for a smaller region of interest (ROI) closer to the transducer face in the pre- and post-compression echo frames to estimate the degree of echo decorrelation present between them. Typically, it is assumed that the post-compression RF signal is a compressed and time-delayed version of the pre-compression counterpart (Hussain et al. 2012a). We then stretch the post-compression signals in the ROI by a varying factor α, that is, $I_\alpha(i) = I_2(\alpha i)$, and define the normalized cross-correlation (NCC) $\rho_\alpha(k)$ (≤ 1) as (Hussain et al. 2012a)

$$\rho_\alpha(k) = \frac{\sum_{i=1}^{L} I_1(i) \cdot I_\alpha(i+k)}{\sqrt{\sum_{i=1}^{L} \{I_1(i)\}^2 \sum_{i=1}^{L} \{I_\alpha(i)\}^2}} \tag{4}$$

where L is the length of a 1-D signal window, and k is the shift parameter. Equation (4) becomes maximum for that particular value of α for which the post-compression RF window matches best with its pre-compression counterpart. After estimating $\rho_\alpha(k)$ for all the scan lines inside the ROI, the mean NCC peak is estimated as

$$\rho_{avg} = \frac{1}{M} \sum_{w=1}^{M} \max\{\rho_\alpha(k)\}_w \tag{5}$$

where M is the total number of 1-D signal windows inside the ROI. Because we want the weight λ to be determined by features of the image, we define it as

$$\lambda = \begin{cases} a & \text{if} \quad \rho_{avg} \geq 0.9 \\ b(\rho_{avg} - a) & \text{if} \quad 0.5 \leq \rho_{avg} < 0.9 \\ 0 & \text{if} \quad \rho_{avg} < 0.5 \end{cases} \tag{6}$$

where $a = 0.5$ and $b = 5/4$, which are chosen such that the linear weight λ (proportional to the echo decorrelation) is clipped at $\rho_{avg} = 0.5$ and $\rho_{avg} = 0.9$. We choose these threshold values because echo decorrelation between the pre- and post-compression echo frames is significantly lower when ρ_{avg} is ≥ 0.9 (Zahiri-Azar and Salcudean 2006). On the other hand, if ρ_{avg} is < 0.5, it is obvious that the degree of echo de-correlation is greater than the correlation (Hussain et al. 2015). After estimating the FM, the location of the maximum intensity point along each scan line of the FM is used as the initial bone surface point estimate $\mathbf{Y}(=[y_1, y_2, \ldots, y_n])$, where y_j is the axial sample number at jth scan line in the FM. We also use Grubbs' test (Nass et al. 2013) to discard any outlier bone candidate point y_j in **Y**.

Single-slice bone detection. To detect a discontinuity in the bone surface, we estimate the least-squares error-based gradient $\nabla\mathbf{Y}$. We assume that the gradient values $\nabla\mathbf{Y}$ are normally distributed with mean $\mu_{\nabla Y}$ and standard deviation $\sigma_{\nabla Y}$. Then we determine if any gradient value is too high by comparing it with the confidence interval of $\mu_{\nabla Y} + 3\sigma_{\nabla Y}$. The locations where $\nabla\mathbf{Y}$ exceeds the confidence interval of $\mu_{\nabla Y} + 3\sigma_{\nabla Y}$ are considered the locations of bone discontinuities. After the discontinuity localization, each continuous portion of points in **Y** is considered as a separate segment, and we use Gaussian mixture regression (GMR) over each of the segments separately. If $f_{X,Y}(x,y) = \sum_{q=1}^{K} \pi_q \phi(x,y;\mu_q,\Sigma_q)$ is the joint density function of bone indicating points in a particular segment of the FM, where K is the total number of clusters present in that segment (K is estimated from spectral clustering [Zelnik-Manor and Perona 2005]), π_q, $\mu_q = [\mu_{qX}; \mu_{qY}]$ and $\Sigma_q = [\Sigma_{qX} \Sigma_{qXY}; \Sigma_{qYX} \Sigma_{qYY}]$ are the probability, mean and covariance matrix, respectively, of the data points in the qth cluster, which are estimated using the expectation maximization algorithm (Cohn et al. 1996). In addition, $\phi(x,y;\mu_q,\Sigma_q)$ is the probability density function of points inside the qth cluster defined as

$$\phi(x,y;\mu_q,\Sigma_q)=\frac{1}{2\pi\sqrt{|\Sigma_q|}}\exp\left[-\frac{1}{2}(D-\mu_q)^T \sum_q^{-1}(D-\mu_q)\right]$$

where $D=[\mathbf{X};\mathbf{Y}]$. Then, from $f_{X,Y}(x,y)$, our GMR equation can be derived (Sung, 2004),

$$b(x)=E[\mathbf{Y}|\mathbf{X}=x]=\sum_{q=1}^{K}w_q(x)d_q(x) \tag{8}$$

where b contains the new bone surface points, $d_q(x)=\mu_{qY}+\sum_{qYX}\sum_{qX}{}^{-1}(x-\mu_{qX})$, and μ_{qX} and Σ_{qX} are the mean and covariance matrix of the marginal density function (f_X) of $\mathbf{X}$, in the qth data cluster. An example plot of b is illustrated in Figure 1 as the "seed bone contour." In addition, $w_j(x)$ is the mixing weight defined as

$$w_q(x)=\frac{\pi_q\phi(x;\mu_{qX},\Sigma_{qX})}{\sum_{q=1}^{K}\pi_q\phi(x;\mu_{qX},\Sigma_{qX})} \tag{9}$$

direction by seeking the depth index in each column of the adjacent frames that minimizes the cost function defined by

$$C(i,j_o,k_o\pm1)=\sum_{j_v=j_o-L_y}^{j_o+L_y}[E_i(i,j_o,k_o\pm1)+\kappa E_s(i,j_o,k_o\pm1)]\times e^{-|j_o-j_v|} \tag{11}$$

where E_i and E_s are the energy functions associated with the new candidate voxel, κ is the mixing weight and L_y is the number of nearest-neighbor lateral voxels. The energy term E_i ensures that the new bone surface voxel at $(j_o,k_o\pm1)$ carries the highest intensity value among the voxels in the interrogated scan line, and is defined as

$$E_i(i,j_o,k_o\pm1)=\frac{1-\left[\widehat{\mathbf{B}}(i,j_o,k_o\pm1)-\mu_t\right]^2-\left[\widehat{\mathbf{B}}(i,j_o,k_o\pm1)-\mu_b\right]^2}{\max\left[1-\left[\widehat{\mathbf{B}}(i,j_o,k_o\pm1)-\mu_t\right]^2-\left[\widehat{\mathbf{B}}(i,j_o,k_o\pm1)-\mu_b\right]^2\right]} \tag{12}$$

3-D bone surface extraction using surface growing

Having identified a seed contour in the 2-D elastographic image, we next use a surface growing approach to extend this contour laterally through the 3-D volume set. Before doing this, we pre-process the 3-D B-mode ($\mathbf{B}$) image to highlight the bone intensities relative to the soft tissues. To do this, we estimate the axially cumulative sum of intensities for each voxel as $P(i,j,k)=\sum_{p_o=1}^{i}\mathbf{B}(p_o,j,k)^2$, where k denotes the voxel index in the elevation direction. Using $P(i,j,k)$, we estimate the modified B-mode volume as

$$\widehat{\mathbf{B}}(i,j,k)=\frac{\mathbf{B}(i,j,k)^{P(i,j,k)}}{\max\left[\mathbf{B}(i,j,k)^{P(i,j,k)}\right]} \tag{10}$$

We assume that the 2-D seed points $b_o(i_o,j_o,k_o)$ correspond to voxels at $(i_o,j_o,z/2)$, where $k_o\approx z/2$. Also note that b_o directly corresponds to b in eqn (8). Then the bone surface expands framewise along the elevation

where

$$\mu_t=\frac{1}{i_t-1}\sum_{a=1}^{i_t-1}\widehat{\mathbf{B}}(i,j_o,k_o\pm1)$$

$$\mu_b=\frac{1}{m-i_b}\sum_{a=i_b+1}^{m}\widehat{\mathbf{B}}(i,j_o,k_o\pm1)$$

and $[i_t,i_b]$ is the axial search range for a new surface candidate centered at i_o. In addition, the energy function E_s ensures a smooth transition between the seed and new candidate voxel, and is defined as

$$E_s(i,j_o,k_o\pm1)=\frac{(|\nabla i|/|\nabla i_t|)^2}{\max\left[(|\nabla i|/|\nabla i_t|)^2\right]} \tag{13}$$

where $\nabla i=i_o-i$ and $\nabla i_t=i_o-i_t$. Finally, we estimate the location of a new bone surface voxel from eqn (11) for the frame at $k_o\pm1$ as

$$i_o|_{k_o\pm1}=\underset{i}{\operatorname{argmin}}\{C(i,j_o,k_o\pm1)\} \tag{14}$$

We update $i_o|_{k_o \pm f}$ as the new seed voxel, proceed to the next frame at $k_o \pm (f+1)$, where $f = 1,2,3\ldots$, and continue growing until $min[C]$ rises to a value that makes it unlikely that the next voxel still represents bone. In our analyses, we set this threshold empirically at a value of 0.8 because we have found that the US bone intensity is too weak to rely on beyond this value; we plan to revisit this choice in the future to base it on a measured property of the image (*e.g.,* average bone intensity). We also store the axial locations of the seed contours b (from eqn [8]) as well as the new surface points (from eqn [14]) in a 2-D matrix B_{est}.

Validation setup

FEM simulation. To validate our proposed approach, we built a 40 × 40-mm (axial × lateral) FEM phantom using the analysis software ANSYS (ANSYS, Canonsburg, PA, USA) and the ultrasound simulation software Field II (Jensen 1996). The phantom mimicked 2-D US scans of a fractured human distal radius bone with a total number of 55,180 nodes. The stiffness values of the homogeneous soft tissue and bone regions were set to 10 kPa and 10 GPa, respectively (Fig. 3), based on a previous related study (Pistoia et al. 2002). Our phantom was compressed in the axial direction from the top using a planar compressor that was wider than the phantom. We simulated an applied pressure level that corresponds to 1% average strain because we have observed in scans of human tissue that there is significant echo decorrelation at strain values beyond this amount (Hussain et al. 2012b). An ultrasonic transducer of center frequency, f_0 = 5 MHz and bandwidth = 50% was used to simulate the phantom scan from the top. The total number of scan lines was set to 128. The resulting pixel size of the 2-D data was 0.015 × 0.3 mm. Figure 3(b) is the simulated elastogram at 1% applied strain. Note that we created this phantom to analyze the performance of different 2-D bone boundary estimation methods only.

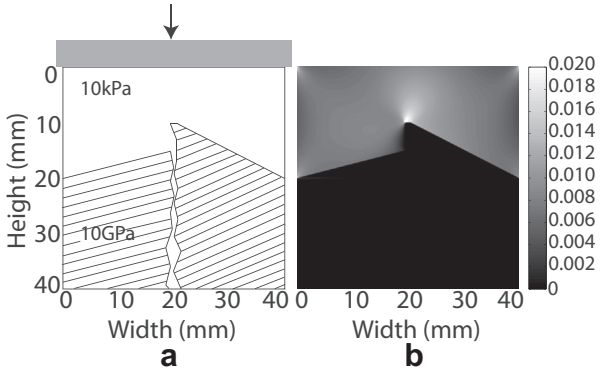

Fig. 3. Finite-element model (FEM) simulation phantom. (a) Model of a fractured distal radius bone and soft tissue region of stiffness 10 GPa and 10 kPa, respectively. (b) Corresponding simulated elastogram.

Experimental phantom. We also constructed an experimental phantom using a radiopaque Sawbones hemipelvis (Sawbones, Pacific Research Laboratories, Vashon Island, WA, USA, Model 1297-22). A portion of the pelvis was suspended in polyvinyl chloride (PVC) gel (Fig. 4a) and placed in an acrylic tube (Fig. 4b). A high-resolution peripheral quantitative CT machine (Model HR pQCT Xtreme CT, Scanco USA, Wayne, PA, USA) was used to acquire a single 482 × 482 × 402 (lateral × axial × elevation) voxel volume with a resolution of 0.25 × 0.25 × 0.25 mm. The US images were acquired using a SonixRP (Ultrasonix Medical, Richmond, BC, Canada) scanner in the Center for Hip Health and Mobility, Vancouver Coastal Health Authority, Vancouver, BC, Canada. We used a L14-5/60 linear array probe operating at 10 MHz and a 4 DL14-5/38 linear 4-D array probe operating at 5 MHz to collect data for the 2-D and 3-D implementations, respectively.

In vivo *data.* Finally, we acquired eight sets of *in vivo* US data, five of which were acquired for 2-D evaluations from five volunteers (volunteer I: 25-y-old man, volunteer II: 33-y-old man, volunteer III: 26-y-old man, volunteer IV: 24-y-old man, volunteer V: 27-y-old man), and three sets of data were acquired for 3-D evaluations from three volunteers (volunteer VI: 27-y-old man, volunteer VII: 26-y-old man, volunteer VIII: 29-y-old man) after obtaining informed consent. All data were acquired with free-hand compression. The US images were acquired using a SonixRP (Ultrasonix Medical) scanner in the Center for Hip Health and Mobility, Vancouver Coastal Health Authority. Here also, we used a L14-5/60 linear array probe operating at 10 MHz and a 4DL14-5/38 linear 4-D array probe operating at 5 MHz to collect data for the 2-D and 3-D implementations, respectively. The study was approved by the UBC clinical research ethics board.

Data analysis

We provide comparative results of our proposed 2-D and 3-D strain enhancement (2DSE and 3DSE) methods with the previously reported adaptively parameterized ("optimized") phase symmetry methods in both two and three dimensions (2DOPS and 3DOPS [Hacihaliloglu et al. 2011 and 2014, respectively]). Note that the 2DSE method refers only to what we proposed in under 2-D Bone Contour Estimation, but the 3DSE method combines methods described under both 2-D Bone Contour Estimation and 3-D Bone Surface Extraction Using Surface Growing. The 2DOPS and 3DOPS methods select parameters automatically for the log-Gabor filters based on properties estimated directly from the specific US image that is being analyzed, as described in Hacihaliloglu et al. (2011, 2014). Because the FEM and physical phantoms do not contain any soft tissue layers above the bone surface, we illustrate the effect of using the depth-

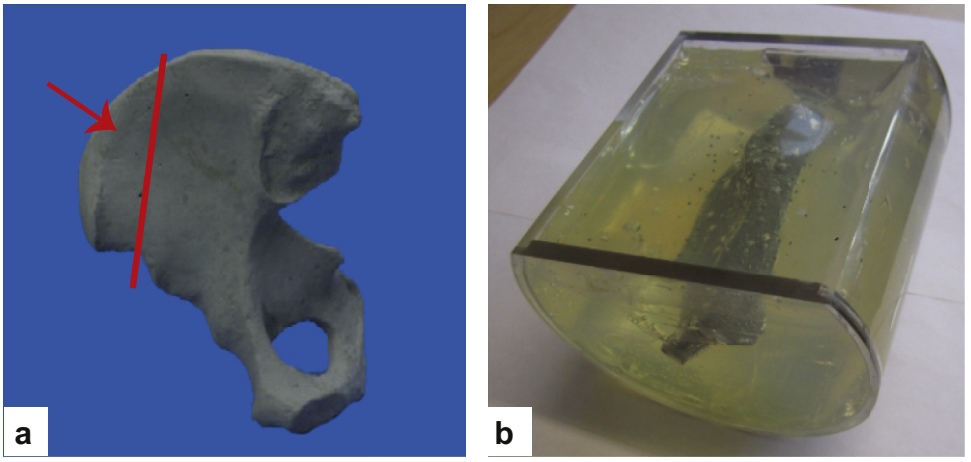

Fig. 4. Experimental physical phantom. (a) The phantom was created using a Sawbones radiopaque hemipelvis, cut along *red line*. (b) The separated portion (indicated by the *red arrow* in a) of the pelvis is embedded in polyvinyl chloride gel.

dependent cumulative power, data-driven weight and GMR in terms of the mean absolute fitting error (MAFE) only for the *in vivo* data. For the FEM and physical phantoms, we calculate the mean absolute error (MAE) relative to a reference bone boundary using

$$\mathrm{MAE} = \frac{1}{P \times Q} \sum_{p=1}^{P} \sum_{q=1}^{Q} \left| B_{\mathrm{ref}}(p,q) - B_{\mathrm{est}}(p,q) \right| \qquad (15)$$

where P and Q represent the number of data points spanned by the bone boundary in the lateral and elevation directions, respectively, and B_{ref} is a matrix containing the "ground truth" bone boundary points. In estimating the MAE for the 2-D cases, we set Q to 1 in eqn (15). As ground truth, we use the estimated bone boundary from the CT image for the experimental phantom and expert delineation of bone boundaries on B-mode images for

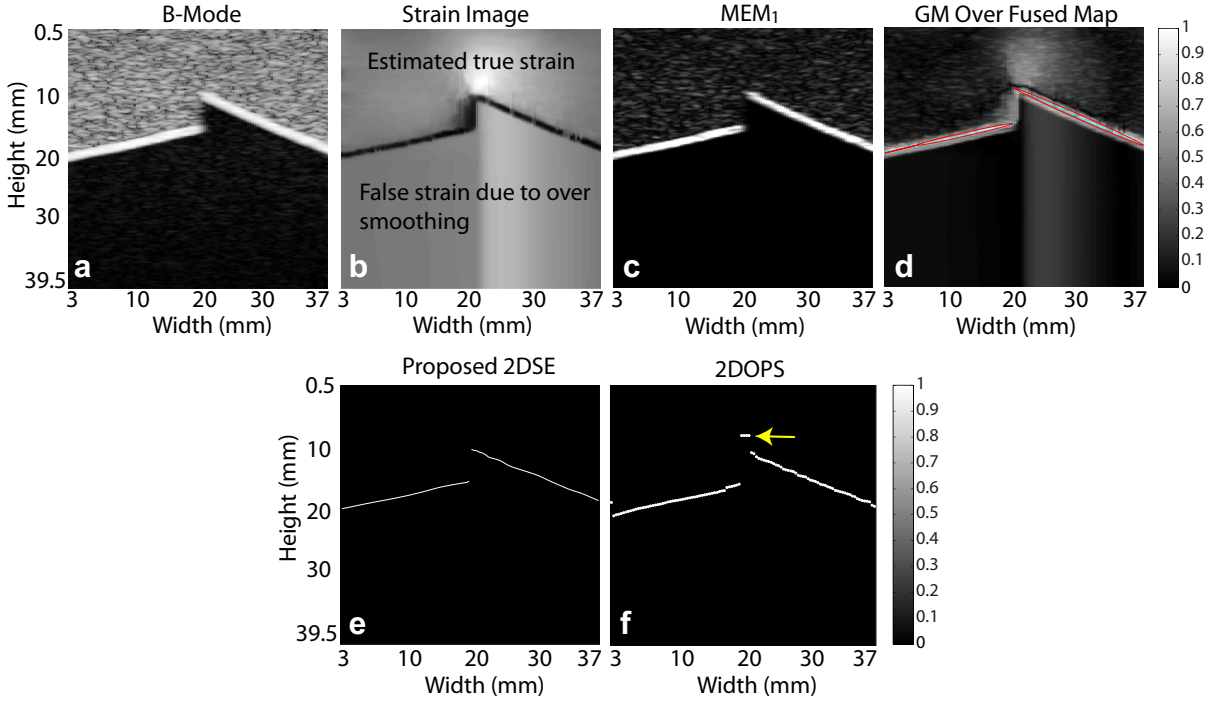

Fig. 5. Two-dimensional bone boundary detection using the finite-element model (FEM) phantom. (a) B-mode image. (b) Strain image generated by the proposed approach. (c) MEM_1. (d) Gaussian mixture (GM) representation over the maximum intensity points in the fused map. (e,f) Bone boundary estimated with the (e) 2-D strain enhancement (2DSE) and (f) 2-D optimized phase symmetry (2DOPS) methods (Hacihaliloglu et al. 2011) (*arrow* indicates leakage). The bone boundary for the 2DOPS method is found using bottom-up ray casting. *Yellow arrow* highlights error in surface estimate.

the *in vivo* data. We use fiducial-based CT and US bone alignment before estimating the MAE for the experimental phantom. Note that we use bottom-up ray casting in the phase symmetry images for the 2DOPS and 3DOPS methods to get B_{est}, as suggested in Hacihaliloglu et al. (2011, 2014). Also note that because we use expert delineated bone contours as ground truth for the *in vivo* data, the estimated error using eqn (15) for the *in vivo* data is more properly considered to be the mean absolute fitting error (MAFE). In our surface growing technique, we set $\nabla i_t \approx 5$ mm, $L_y = 3$ and $\kappa = 0.5$.

RESULTS

Validation on the FEM phantom data

Figure 5 illustrates a comparison of the 2DSE and 2DOPS algorithms when applied to the FEM phantom. In Figure 5(a–d), we have the B-mode, estimated strain **S**, MEM_1 and fused maps, respectively. In Figure 5(e), we have the bone boundaries detected by the 2DSE method. In addition, we have the bone boundaries detected by the 2DOPS method in Figure 5(f). Note that because the FEM and experimental phantom data by default contain no different tissue layers in the soft tissue region, the estimated bone boundaries by the 2DOPS method have very few false positives. However, as the 2DOPS method depends on ray casting to extract the final bone boundary from the phase symmetry images, these methods become vulnerable to "leaking" through weak areas in the phase symmetry profiles, as is evident in Figure 5(f) (indicated by *yellow arrows*). In contrast, the bone boundaries produced by the 2DSE method (Fig. 5e) appear to be free of such artifacts.

Validation on the physical phantom data

Qualitative performance comparison. Figure 6 illustrates the qualitative performance comparison of the 2DSE and 2DOPS methods using the experimental phantom. In Figure 6(a–d) are the B-mode image, strain image, MEM_1, and fused map, respectively. The detected bone boundaries by the 2DSE and 2DOPS methods are in Figure 6(e and f, respectively). We can see from Figure 6(f) that the final bone boundary estimated by the 2DOPS method is somewhat noisy, though a GMR operation on these points might produce a smooth contour as with the 2DSE method (Fig. 6f). But we see in Figure 7 for the 3DOPS method that the ray casting leaks through weak spots (indicated by *white arrows*) in the

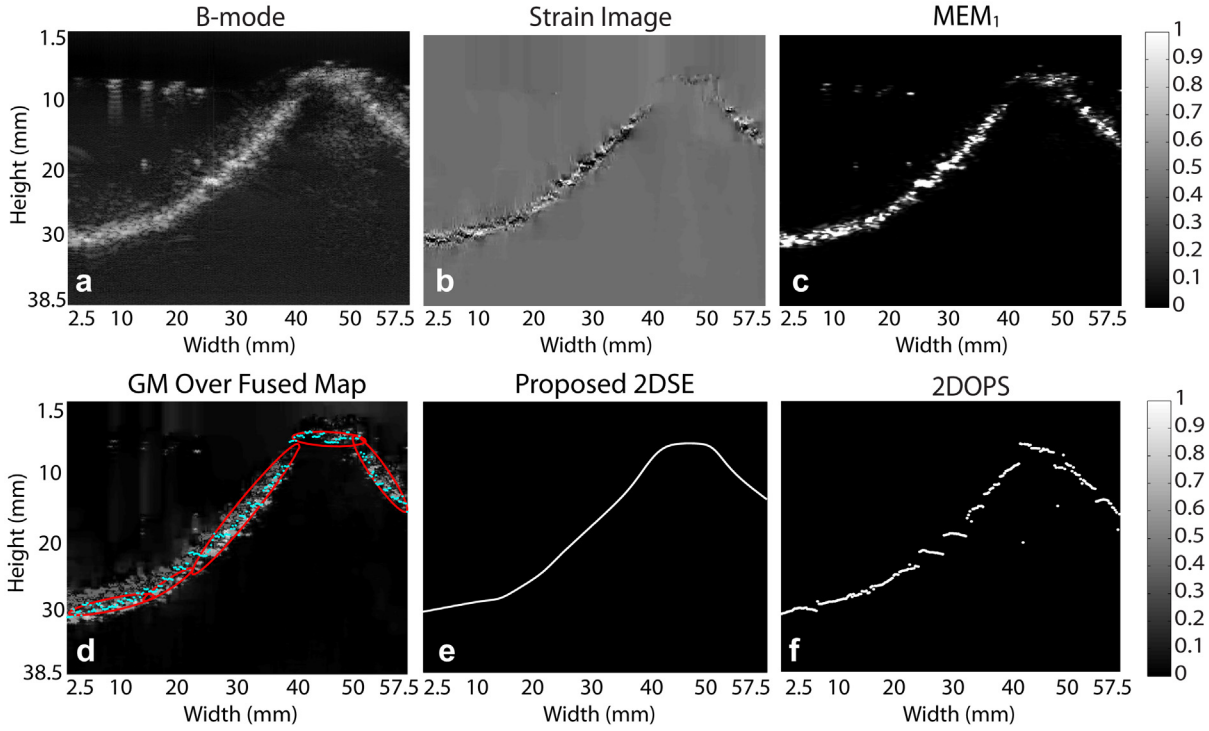

Fig. 6. Two-dimensional bone boundary detection using the physical phantom. (a) B-Mode image. (b) Strain image generated by the proposed approach. (c) MEM_1. (d) Gaussian mixture (GM) representation over the maximum intensity points in the fused map. (e) Bone boundary estimated with the 2-D strain enhancement (2DSE) method. (f) Bone boundary estimated with the 2-D optimized phase symmetry (2DOPS) method (Hacihaliloglu et al. 2011) (bone boundary is shown after bottom-up ray casting).

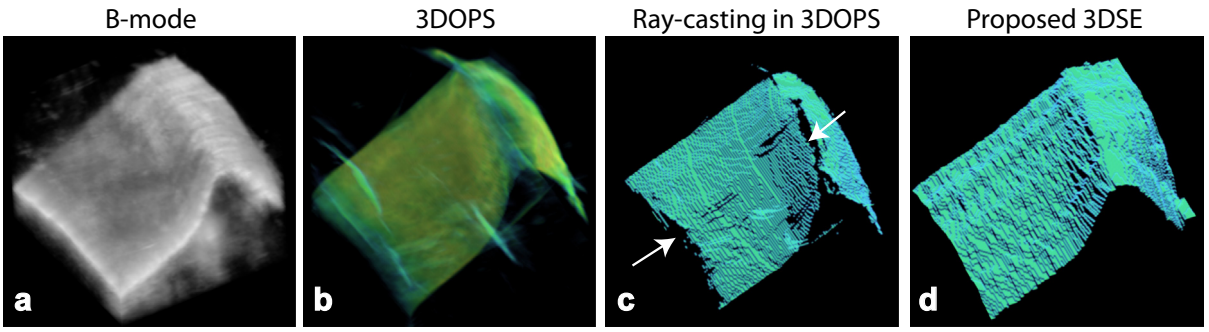

Fig. 7. Three-dimensional bone surface detection using the physical phantom. (a) B-Mode image. (b) Three-dimensional phase symmetry image estimated with the 3-D optimized phase symmetry (3DOPS) method (Hacihaliloglu et al. 2014). (c) Bone surface after bottom-up ray casting in (b) (*arrows* indicate leakage). (d) Bone surface estimated with the 3-D strain enhancement (3DSE) method.

3-D phase symmetry image. Although for the sake of clarity, we do not indicate the false positives on top of the bone surface resulting from leaking, such false positives may be difficult to identify and reject automatically in intra-operative applications. In contrast, the bone surface estimated by the 3DSE has no leaking effect (Fig. 7d).

Quantitative performance comparison. We also compared the quantitative performance on the phantom data between the OPS and SE methods in both two and three dimensions. There were average decreases in the MAE of 18% and 23%, respectively, for the 2DSE and 3DSE methods compared with their OPS equivalents.

Validation on the in vivo *data*

Qualitative performance comparison. First, we compared the bone boundary detection performance of the 2DSE and 2DOPS methods using the *in vivo* data. The scanned bone regions on the anatomies and the B-mode images of volunteers I–V are provided in Figure 8(a–e) and Figure 8(u–y), respectively. An orthopedic surgeon delineated the bone boundaries on the B-mode images (Fig. 8u–y), which we treat as ground truths for comparing the 2DSE and 2DOPS methods. We see from Figure 8(u–y) that the bone boundary produced by the 2DOPS method varies noticeably in some places. This variation results from the false-positive bone responses. In contrast, in all five cases, the bone boundaries estimated by the 2DSE method better match the shapes as marked by the expert in the corresponding B-mode images (Fig. 8u–y). In addition, the 2DSE method does not produce false positives at soft tissue interfaces.

We also illustrate the bone surface detection performance of the 3DSE and 3DOPS methods in Figure 9. We see in Figure 9(g–i) that the 3DOPS method can produce false-positive responses at various soft tissue interfaces (indicated by *white arrows*). We also see in Figure 9(j–l) that the ray casting results in leaks through weak responses on the bone surface and instead detects false-positive soft tissue interfaces (indicated by corresponding *white arrows* in Fig. 9g–l). In contrast, in all three cases, the bone surfaces estimated by the 3DSE method better match the shapes visible in the corresponding B-mode images (Fig. 9d–f, m–o). In addition, the 3DSE method successfully extracts bone surfaces that are not perpendicular to the US beam direction (indicated by the corresponding *green arrows* in Fig. 9d, f, m, o). In contrast, the 3DOPS method fails to extract these curved bone regions. Note that the *in vivo* data we used in this study have bone surfaces located at reasonably shallow depths (within $\sim$ 3 cm of the surface). However, in principle, our technique should work for deeper bones provided that the surface is satisfactorily visualized in the B-mode images.

Quantitative performance comparison. We illustrate a quantitative performance comparison between the 2DSE and 2DOPS methods in terms of MAFE in Figure 10(a). The MAFE values produced by the 2DSE method are lower (approximately 55%) than those of the typical 2DOPS (with only ray casting) method for all five volunteer data sets. We also estimate the MAFE for the ray-cast surface points after GMR. Although GMR reduces the error significantly, the errors with 2DSE are even lower (by 0.15 mm on average). In addition to the MAFE, we also analyze the distributions of the estimated bone boundary points by the 2DOPS (without GMR) and 2DSE methods with respect to the expert-delineated bone contours. We perform an F test on the variances of the distributions produced by the 2DOPS and 2DSE methods, as outlined in Table 1. We see in this table that $F > F$ Critical, one-tailed, which rejects the null hypothesis: variances for the 2DOPS and 2DSE methods are equal. Thus, the variance for the 2DOPS method is greater than that of the 2DSE method. We also illustrate the quantitative performance comparison

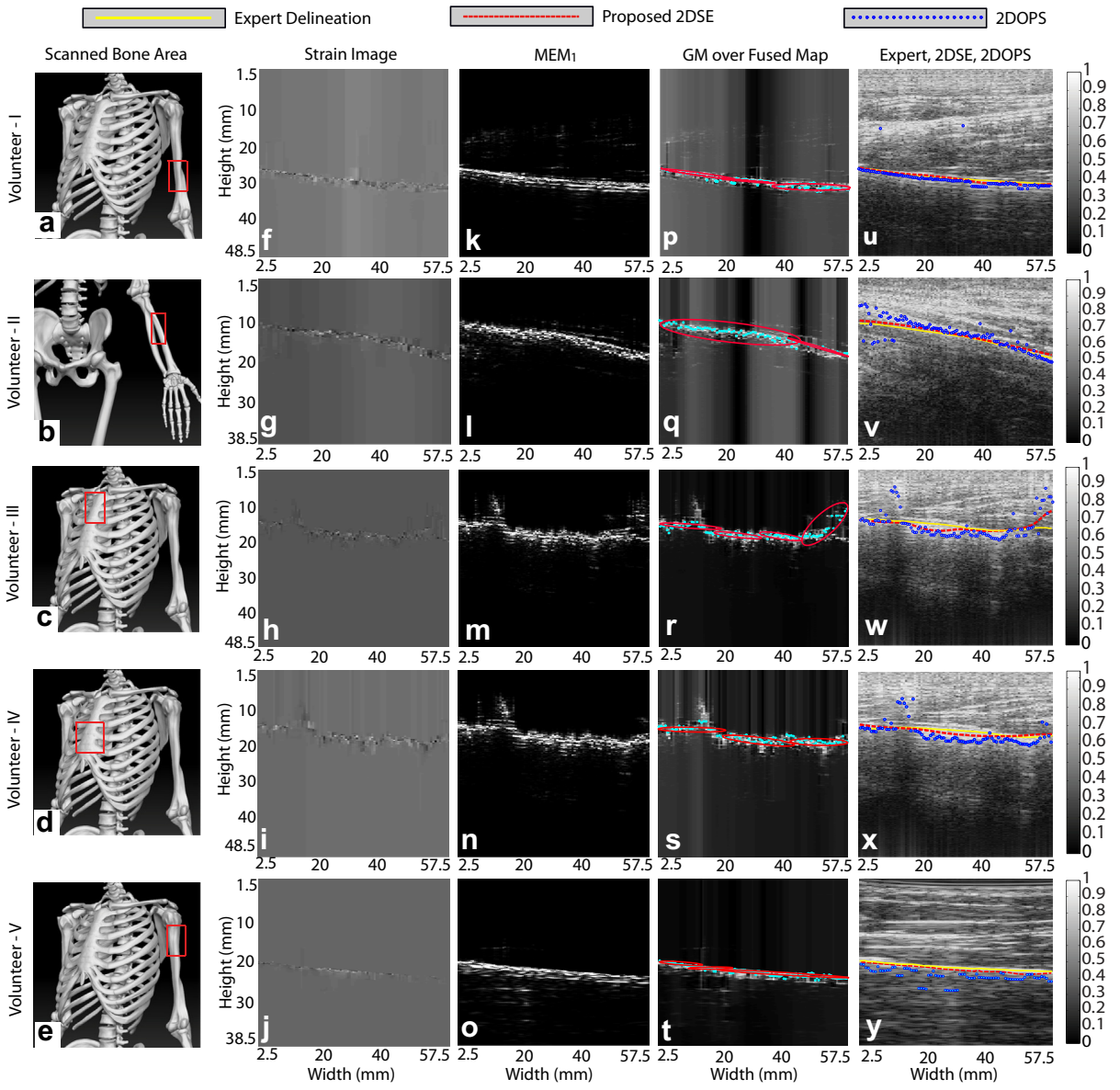

Fig. 8. Two-dimensional bone boundary detection using the *in vivo* data. (a–e) Bone regions scanned on each volunteer (with *red rectangles*). (f–j) Strain images generated by the proposed approach. (k–o) MEM_1. (p–t) Fused maps with the Gaussian mixtures (GM) overlaid on the maximum intensity points. (u–y) Orthopedic expert-delineated bone boundaries and bone boundaries detected with 2-D optimized phase symmetry (2DOPS) (Hacihaliloglu et al. 2011) and 2-D strain enhancement (2DSE) methods are overlaid on the respective B-mode images for volunteers I to V (bone boundaries produced by the 2DOPS method are shown after bottom-up ray casting).

between the 3DSE and 3DOPS methods in terms of computation time in Figure 10(b). The MATLAB (The MathWorks, Natick, MA, USA) execution times for the 3DSE method running on an Intel(R) Xeon(R) CPU E3 @ 3.20 GHz with 8 GB of memory are approximately 18 times smaller than those of the 3DOPS method for all three 3-D *in vivo* data sets.

Finally, we illustrate the individual effect of using the depth-dependent cumulative power, data-driven weight and GMR in terms of MAFE using the *in vivo* data in Figure 11. Because we enhanced our previous work (Hussain et al. 2014), namely, the strain and envelope power-based method (SEP), we illustrate the effects of the proposed enhancements with the SEP method. To illustrate the effect of using the depth-dependent cumulative power, we choose a pair of pre- and post-compression RF frames having satisfactory correlation (*i.e.*, $\rho_{avg} \approx 0.90$) and use simple linear regression for both the 2DSE and SEP methods (Fig. 11a). We see that the depth-dependent

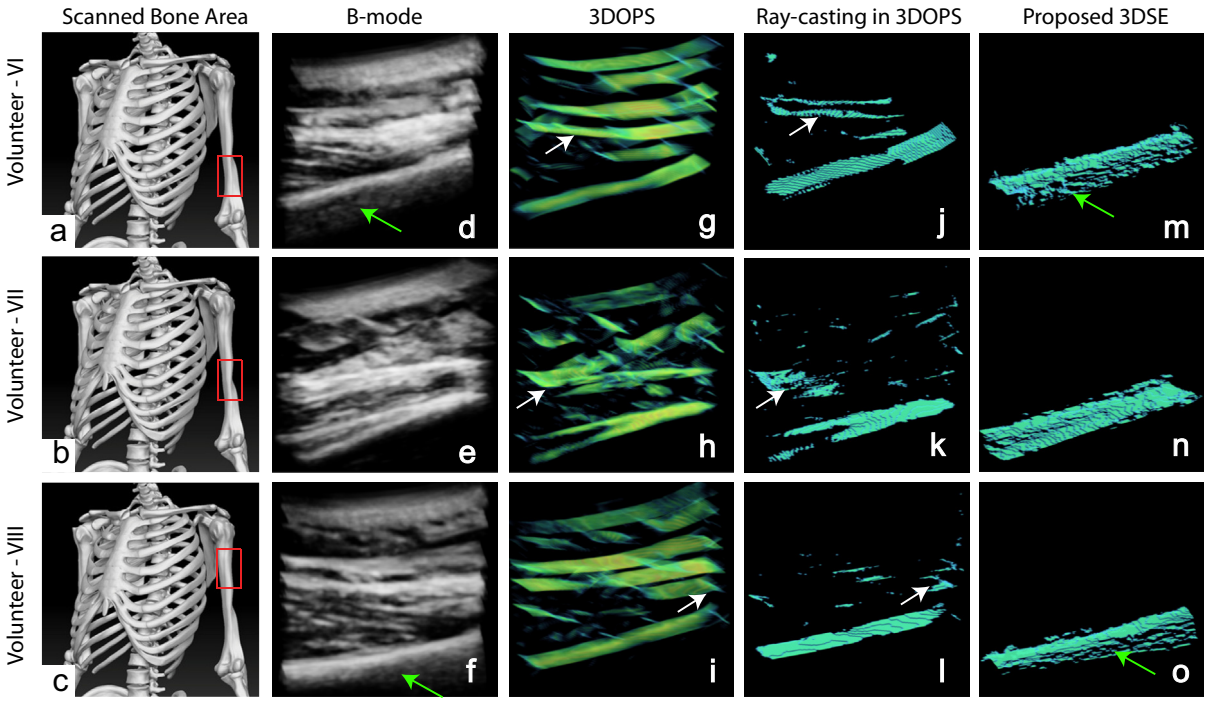

Fig. 9. Three-dimensional bone surface detection using *in vivo* data. (a–c) Bone regions scanned on each volunteer (with *red rectangles*). (d–f) B-Mode images. (g–i) Three-dimensional phase symmetry images estimated with the 3-D optimized phase symmetry (3DOPS) method (Hacihaliloglu et al. 2014). (j–l) Bone surface after bottom-up ray casting in (g)–(i), respectively. (m–o) Bone surfaces estimated with the 3-D strain enhancement (3DSE) method.

cumulative power reduces the MAFE for the 2DSE method by approximately 15% compared with the SEP method. On the other hand, although we illustrate the effect of using a value for λ determined by the degree of correlation, we do not use the depth-dependent cumulative power and use simple linear regression for both the 2DSE and SEP methods (Fig. 11b, c). Here we see that the use of $\lambda(\rho_{avg})$ reduces the MAFE for the 2DSE method by approximately 20% compared with the SEP method. Finally, to illustrate the effect of using the GMR, we use GMR and linear regression separately for the 2DSE method (Fig. 11d). We see that the use of GMR reduces the MAFE for the 2DSE method by approximately 16% compared with the SEP method. We therefore conclude that all three aspects of the method contribute significantly to reducing error, with the use of $\lambda(\rho_{avg})$ having the greatest impact.

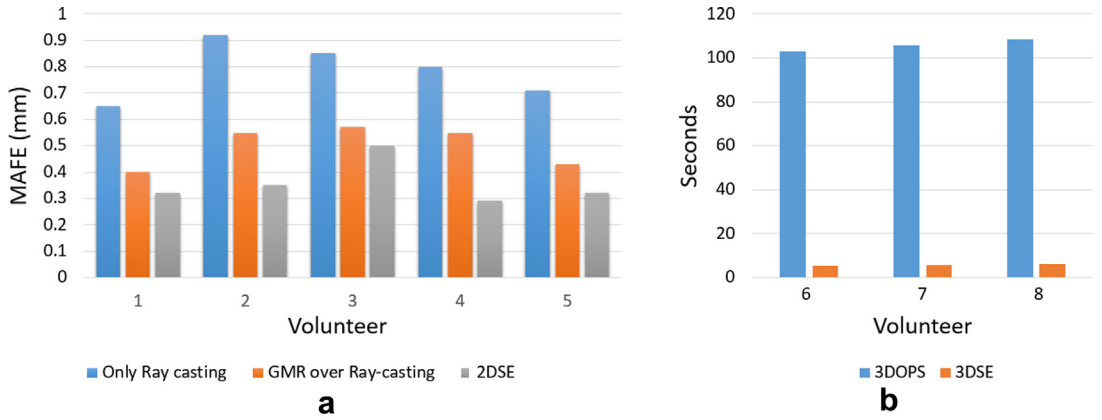

Fig. 10. (a) Mean absolute fitting error (MAFE, mm) analysis for the proposed 2-D strain enhancement (2DSE) and 2-D optimized phase symmetry (2DOPS) methods. (b) Computation time (sec) performance comparisons between the 3DSE and 3DOPS methods using the *in vivo* data. In (b), the 3-D image volume size was 364 × 110 × 50 voxels.

Table 1. F test on the variances of the estimated bone boundary points with respect to the expert delineated bone contours

Source	2DOPS method	2DSE method
Mean	5.118	0.896
Variance	8.36967	0.72568
Observations	5	5
Degrees of freedom	4	4
F	11.5336	
P ($F \leq f$), one-tailed	0.01808	
F critical, one-tailed	6.38823	

2DOPS = 2-D optimized phase symmetry, 2DSE = 2-D strain enhancement.

DISCUSSION

We have proposed an improved 2-D bone segmentation method that (i) incorporates a depth-dependent cumulative power of the envelope into the elastographic data, (ii) uses an automatic weight based on the echo decorrelation measure between the pre- and post-compression RF frames to fuse the strain and envelope power map and (iii) uses a local statistics-based bone discontinuity detection scheme. (iv) We also extend our 2-D bone contour into a 3-D bone surface by using an effective surface growing-based approach. Our method achieved a marked reduction of false-positive bone

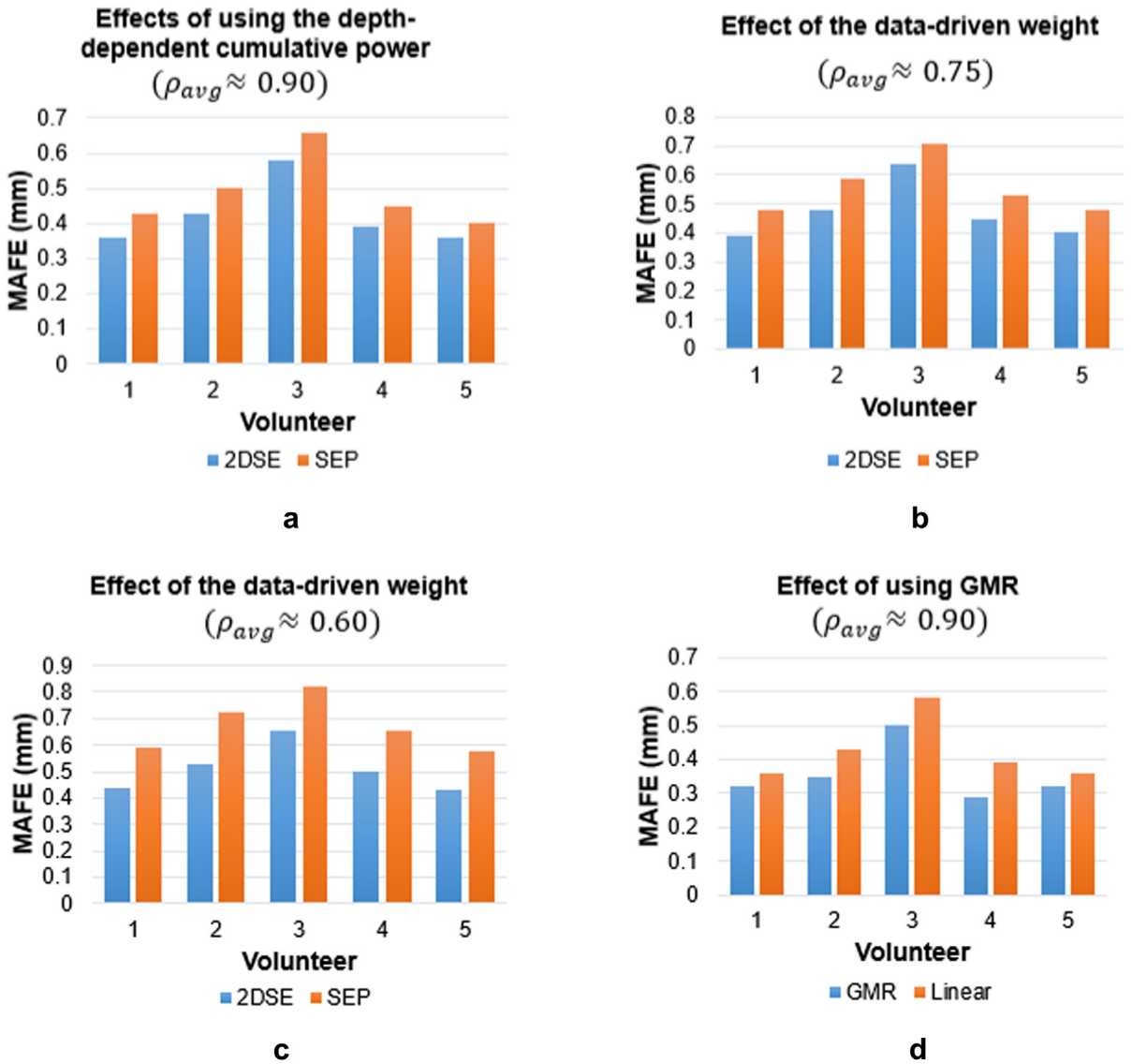

Fig. 11. Mean absolute fitting error (MAFE, mm) analysis reflecting the individual effects of using the (a) depth-dependent cumulative power (at $\rho_{avg} \approx 0.90$), (b, c) Data-driven weight (at $\rho_{avg} \approx 0.75$ and 0.60, respectively). (d) Gaussian mixture regression (GMR) on the *in vivo* data.

responses at the soft tissue interfaces compared with the phase symmetry-based state-of-the-art methods. In addition, our 3-D method was found to be robust in bone segmentation, as well as time efficient, compared with the state-of-the-art methods. We have illustrated our improved performance on a wide range of validation data including the FEM phantom, a physical phantom and *in vivo* human data. We have achieved improvements of approximately 18% on the 2-D physical phantom and 23% on the 3-D physical phantom in terms of MAE compared with current phase feature-based methods. In addition, we have achieved an improvement of approximately 55% on the 2-D *in vivo* data in terms of MAFE compared with current phase feature-based state-of-the-art techniques. We have also performed 3-D bone segmentation on *in vivo* data approximately 18 times faster than the current state-of-the-art method.

We anticipate some situations that could potentially be challenging for our proposed methods:

Non-displaced fractures and small bone defects

Because the 2DSE method identifies any bone discontinuity before the GMR step, it is possible to effectively identify bone fragments that are displaced relative to each other by distances of as little as 2–3 pixels. However, if the fracture is relatively non-displaced, it may not be detected. In addition, if a typical bone defect is very small and lies very close to the actual bone surface, then this defect may be lost during GMR.

Operator dependence in strain imaging

In principle and in practice, our technique can be sensitive to the skill level of the operator because the strain images require that the images used to estimate strain remain substantially coplanar. Although we did not explicitly evaluate this operator dependence, we did observe that relatively naïve operators (*e.g.,* other lab members) could quickly be trained to produce satisfactory strain images by adopting either of two very easy approaches, depending on the capability of the US machine:

1. Machines that support strain imaging: If a machine can display both a B-mode image and a corresponding strain image side-by-side in a single display, the operator can visually correlate anatomic features (*e.g.,* the bone surface) between two different images. If an operator observes a low strain profile along what they believe to be the actual bone surface, then he or she can select these images for detailed processing.
2. Machines lacking strain imaging: Our approach can be applied off-line if the machine does not explicitly support strain imaging. In this situation, the operator must pay careful attention during the compression process to ensure that there are no feature changes during this process. Although this is technically a source of operator dependence, we did not observe operators having any obviously significant difficulties acquiring acceptable images, but we have not explicitly measured the size of this effect.

Acknowledgments—We acknowledge the Natural Sciences and Engineering Research Council of Canada (NSERC) for Grants 034685 and 034813 (UBC), which supported this project. We also thank the Centre for Hip Health and Mobility for providing the lab facilities and the Institute for Computing, Information and Cognitive Systems for program support.

REFERENCES

Alfiansyah A, Streichenberger R, Kilian P, Bellemare M, Coulon O. Automatic segmentation of hip bone surface in ultrasound images using an active contour. Int J Comput Assisted Radiol Surg 2006;1:496.

Amin DV, Kanade T, Digioia AM, Jaramaz B. Ultrasound registration of the bone surface for surgical navigation. Comput Aided Surg 2003; 8:1–16.

Barratt DC, Penney GP, Chan CS, Slomczykowski M, Carter TJ, Edwards PJ, Hawkes DJ. Self-calibrating 3D-ultrasound-based bone registration for minimally invasive orthopedic surgery. IEEE Trans Med Imaging 2006;25:312–323.

Brendel B, Winter S, Rick A, Stockheim M, Ermert H. Registration of 3D CT and ultrasound datasets of the spine using bone structures. Comput Aided Surg 2002;7:146–155.

Brounstein A, Hacihaliloglu I, Guy P, Hodgson A, Abugharbieh R. Towards real-time 3D US to CT bone image registration using phase and curvature feature based GMM matching. In: Medical Image Computing and Computer-Assisted Intervention—MICCAI 2011. Springer, Toronto, Canada; 2011. p. 235–242.

Chen TK, Abolmaesumi P, Pichora DR, Ellis RE. A system for ultrasound-guided computer-assisted orthopaedic surgery. Comput Aided Surg 2005;10:281–292.

Cohn DA, Ghahramani Z, Jordan MI. Active learning with statistical models. J Artif Intell Res 1996;4:129–145.

Daanen V, Tonetti J, Troccaz J. A fully automated method for the delineation of osseous interface in ultrasound images. In: Medical Image Computing and Computer-Assisted Intervention—MICCAI 2004. Springer, Rennes, Saint Malo, France; 2004. p. 549–557.

Foroughi P, Boctor E, Swartz MJ, Taylor RH, Fichtinger G. Ultrasound bone segmentation using dynamic programming. Proc IEEE Ultrason Symp 2007;2523–2526.

Hacihaliloglu I, Abugharbieh R, Hodgson AJ, Guy P. Automatic bone contour detection in 3D B-mode ultrasound images using optimized phase symmetry features: A clinical evaluation evaluation for pelvic fracture. J Bone Jt Surg Br 2012a;94B(Suppl. XLIV):64.

Hacihaliloglu I, Abugharbieh R, Hodgson A, Rohling R. Bone segmentation and fracture detection in ultrasound using 3D local phase features. In: Medical Image Computing and Computer-Assisted Intervention—MICCAI 2008. Springer, New York, USA; 2008. p. 287–295.

Hacihaliloglu I, Abugharbieh R, Hodgson AJ, Rohling RN. Automatic adaptive parameterization in local phase feature-based bone segmentation in ultrasound. Ultrasound Med Biol 2011;37:1689–1703.

Hacihaliloglu I, Brounstein A, Guy P, Hodgson A, Abugharbieh R. 3D ultrasound-CT registration in orthopaedic trauma using GMM registration with optimized particle simulation-based data reduction. In: Medical Image Computing and Computer-Assisted Intervention—MICCAI 2012. Springer, Nice, France; 2012b. p. 82–89.

Hacihaliloglu I, Guy P, Hodgson AJ, Abugharbieh R. Volume-specific parameter optimization of 3D local phase features for improved extraction of bone surfaces in ultrasound. Int J Med Robot 2014;10:461–473.

Hussain MA, Abu Anas EM, Alam SK, Lee SY, Hasan MK. Direct and gradient-based average strain estimation by using weighted nearest neighbor cross-correlation peaks. IEEE Trans Ultrason Ferroelectr Freq Control 2012a;59:1713–1728.

Hussain MA, Alam SK, Lee SY, Hasan MK. Robust strain-estimation algorithm using combined radiofrequency and envelope cross-correlation with diffusion filtering. Ultrason Imaging 2012b;34: 93–109.

Hussain MA, Guy P, Hodgson AJ, Abugharbieh R. Automatic bone segmentation in ultrasound using combined ultrasound strain imaging and envelope signal power. In: 15th Annual Meeting of International Society for Computer Assisted Orthopedic Surgery (CAOS) Society. CAOS Society, Vancouver, Canada; 2015.

Hussain MA, Hodgson A, Abugharbieh R. Robust bone detection in ultrasound using combined strain imaging and envelope signal power detection. In: Medical Image Computing and Computer-Assisted Intervention—MICCAI 2014. Springer, Boston, MA, USA; 2014. p. 356–363.

Jain AK, Taylor RH. Understanding bone responses in B-mode ultrasound images and automatic bone surface extraction using a Bayesian probabilistic framework. Proc SPIE 2004;5373:131–142.

Jensen JA. Field: A program for simulating ultrasound systems. Paper presented at 10th Nordicbaltic Conference on Biomedical Imaging, Part 1. Med Biol Eng Comput 1996;34(Suppl. 1):351–353.

Kowal J, Amstutz C, Langlotz F, Talib H, Ballester MG. Automated bone contour detection in ultrasound B-mode images for minimally invasive registration in computer-assisted surgery An in vitro evaluation. Int J Med Robot 2007;3:341–348.

Krissian K, Westin CF, Kikinis R, Vosburgh KG. Oriented speckle reducing anisotropic diffusion. IEEE Trans Image Process 2007; 16:1412–1424.

Nass R, Farhy LS, Liu J, Pezzoli SS, Johnson ML, Gaylinn BD, Thorner MO. Age-dependent decline in acyl-ghrelin concentrations and reduced association of acyl-ghrelin and growth hormone in healthy older adults. J Clin Endocrinol Metab 2013;99:602–608.

Park MS, Lee KM, Lee B, Min E, Kim Y, Jeon S, Huh Y, Lee K. Comparison of operator radiation exposure between C-arm and O-arm fluoroscopy for orthopaedic surgery. Radiat Prot Dosimetry 2012; 148:431–438.

Patwardhan KA, Cao K, Mills D, Thiele R. Automated bone and joint-region segmentation in volumetric ultrasound. In: Proceedings, 9th IEEE International Symposium on Biomedical Imaging (ISBI). New York: IEEE; 2012. p. 1327–1330.

Pistoia W, Van Rietbergen B, Lochmüller EM, Lill C, Eckstein F, Rüegsegger P. Estimation of distal radius failure load with micro-finite element analysis models based on three-dimensional peripheral quantitative computed tomography images. Bone 2002;30: 842–848.

Rivaz H, Boctor EM, Choti MA, Hager GD. Real-time regularized ultrasound elastography. IEEE Trans Med Imaging 2011;30: 928–945.

Stindel E, Briard J, Merloz P, Plaweski S, Dubrana F, Lefevre C, Troccaz J. Bone morphing: 3D morphological data for total knee arthroplasty. Comput Aided Surg 2002;7:156–168.

Sung HG. Gaussian mixture regression and classification. PhD thesis, Rice University, Houston, TX, USA; 2004.

Tonetti J, Carrat L, Blendea S, Merloz P, Troccaz J, Lavallée S, Chirossel JP. Clinical results of percutaneous pelvic surgery: Computer assisted surgery using ultrasound compared to standard fluoroscopy. Comput Aided Surg 2001;6:204–211.

Xu W, Salcudean ST. Enhancement of bone surface visualization using ultrasound radio-frequency signals. Proc IEEE Ultrason Symp 2007;2535–2538.

Zahiri-Azar R, Salcudean SE. Motion estimation in ultrasound images using time domain cross correlation with prior estimates. IEEE Trans Biomed Eng 2006;53:1990–2000.

Zelnik-Manor L, Perona P. Self-tuning spectral clustering. In: Saul LK, Weiss Y, Bottou L, (eds). Advances in neural information processing systems: Proceedings of the 2004 conference. Cambridge, MA: MIT Press; 2005. p. 1601–1608.